Article

D-orbital Reconstruction Achieves Low Charge Overpotential in Li-oxygen Batteries

Yin Zhou[1,5], Kun Yin[2,5], Yingying Huang[1], Jiapei Li[1], Anquan Zhu[1], Dewu Lin[1], Guoqiang Gan[1], Jianfang Zhang[1], Kai Liu[1], Tian Zhang[1], Kunlun Liu[1], Chuhao Luan[1], Huawei Yang[2], Hou Chen[2], Shaojun Guo [3] ✉, Wenjun Zhang [1] ✉ & Guo Hong [1,4] ✉

Charge overpotential for oxygen evolution reaction is a crucial parameter for the energy conversion efficiency of lithium-oxygen (Li-O_2) batteries. So far, the realization of low charge overpotential via catalyst design is a grand challenge in this field, which usually exceeds 0.25 V. Herein, we report an orbital reconstruction strategy to significantly decrease the charge overpotential to the low 0.11 V by employing PdCo nanosheet catalyst under a low-loading mass (0.3 mg/cm^2) and capacity (0.3 mAh/cm^2). Experimental and theoretical calculations demonstrate that the precise d-d orbital coupling (d_{xz}-d_{xz}, d_{yz}-d_{yz} and d_z^2-d_z^2) between the low-electronegativity Co and Pd leads to the reconstruction of Pd 4d orbitals in PdCo nanosheets, thereby resulting in a downward shift of all the three active Pd 4d orbitals (d_z^2, d_{xz} and d_{yz}) relative to that of Pd nanosheets. Furthermore, the highest energy level of the Pd 4d_z^2 orbital in PdCo is lower than the lowest energy levels of the Pd 4d_{xz} and 4d_{yz} orbitals in pure Pd, significantly decreasing the charge activation energy and achieving a highest energy conversion efficiency of 91%. This finding provides the orbital-level tuning into rational design of highly efficient electrocatalysts for Li-O_2 batteries.

Lithium-oxygen (Li-O_2) battery has garnered wide attention due to its highest theoretical energy density of 3500 Wh kg^{-1} among all the battery systems[1,2], making it a highly promising candidate for the market competition in long-range electric vehicles and massive energy storages[3–7]. However, the sluggish oxygen evolution reaction (OER) leads to high charge overpotential and thus, low energy conversion efficiency, which is the bottleneck problem in the development of Li-O_2 batteries[8–10]. In addition, such high charge overpotential can lead to the degradation of electrolytes and the deposition of insulating parasitic products, causing inferior cycle stability[11–14]. To date, significant efforts have been devoted to reducing the charge overpotential by designing cathode electrocatalysts, such as noble metal-based alloys[15–17], single-atom catalysts[18–21], sulfides[22–24], transition metal oxides[25–27], and metal-organic frameworks[28–31], etc. Recently, Pd-based nanocatalysts are highly considered as the promising candidates for Li-O_2 batteries due to their tunable orbital electronic configuration and energy levels[32–34]. The main strategy for decreasing the charge overpotential of Pd-based catalysts is to reduce the overall d-band energy level (d-band center) of Pd, thereby weakening the adsorption interaction towards intermediate[5,35]. However, only the regulation of the d-band center does not ensure a simultaneous reduction of the three active orbitals (d_{xz}, d_{yz}, and d_z^2) out of the total five orbitals

[1]Department of Materials Science and Engineering & Center of Super-Diamond and Advanced Films, City University of Hong Kong, 83 Tat Chee Avenue, Kowloon, Hong Kong SAR 999077, China. [2]School of Chemistry and Materials Science, Shandong Key University Laboratory of High Performance and Functional Polymer, Ludong University, Yantai 264025, China. [3]School of Materials Science and Engineering, Peking University, Beijing 100871, China. [4]The Shenzhen Research Institute, City University of Hong Kong, Shenzhen 518057, China. [5]These authors contributed equally: Yin Zhou, Kun Yin. ✉e-mail: guosj@pku.edu.cn; WJ.Zhang@cityu.edu.hk; guohong@cityu.edu.hk

(the other two inactive orbitals are $d_{x^2-y^2}$ and d_{xy}). Consequently, the charge overpotentials have not been reduced to the desired value of below 0.25 V, which is the threshold of a reliable battery system with an energy conversion efficiency above 85%[12,34,36,37].

Herein, we propose an orbital reconstruction strategy to remarkably reduce the charge overpotential to 0.11 V by using PdCo at a low loading mass (0.3 mg/cm^2) with a low capacity (0.3 mAh/cm^2). Due to the lower electronegativity of Co over other transition metals, and the perfect alignment of d orbitals between Pd and Co (energy level differences are less than 0.5 eV), the desired d-d orbital coupling of Pd and Co (d_{xz}-d_{xz}, d_{yz}-d_{yz}, and d_{z^2}-d_{z^2}) in PdCo nanosheets induced Pd 4 d orbital reconstruction and effectively lowered the energy levels of the active d_{xz}, d_{yz}, and d_{z^2} orbitals of Pd. Theoretical calculations further indicated that the top energy level of the reconstructed d_{z^2} orbital of Pd in PdCo nanosheets was even lower than the bottom energy level of Pd $d_{xz/yz}$ orbitals in Pd nanosheets, which significantly lowered the activation energy of the OER rate-determining step (LiO$_2$ = Li$^+$ + O$_2$) in Li-O$_2$ batteries and achieved the high energy conversion efficiency of 91%.

Results

Synthesis and characterization of Pd$_{72}$Co$_{28}$ nanosheets

The PdCo nanosheet was synthesized through a conventional colloidal chemistry method. The obtained PdCo nanosheets exhibited a highly curved morphology (Fig. 1a) with a thickness of approximately 3-4 nm in atomic force microscopy (AFM, Fig. 1b). Similarly, Pd nanosheets synthesized by the same method demonstrated a comparable curved morphology and uniform distribution of Pd elements (Supplementary Fig. 1). The X-ray diffraction (XRD) patterns of PdCo nanosheets

showed a slight shift towards lower angles compared to that of Pd nanosheets due to the alloying and tensile strain effect (Fig. 1c). On one hand, due to the slightly smaller radius of Co compared to Pd, the XRD peak of Pd$_{72}$Co$_{28}$ shifts slightly towards higher angles caused by the alloying effect. On the other hand, the thickness of Pd$_{72}$Co$_{28}$ nanosheets is about 0.9 nm less than that of Pd nanosheets (Supplementary Fig. 1d), resulting in a stronger tensile strain effect. Consequently, the XRD peak of PdCo notably shifts towards lower angles compared to the Pd nanosheets. Therefore, the weak alloying effect and the strong tensile strain effect resulted in the XRD peak of Pd$_{72}$Co$_{28}$ shifting towards lower angles compared to the Pd nanosheet. The fast Fourier transform (FFT) analysis of PdCo nanosheets from the selected white dashed region exhibited distinct crystal facets oriented along the [011] zone axis (Fig. 1d), which aligned with the results from the XRD patterns. The lattice spacing of 0.248 nm observed in the high-angle annular dark-field scanning TEM (HAADF-STEM) corresponded to the (111) facets of PdCo (Fig. 1d, e). The line scan analysis and energy-dispersive X-ray spectroscopy (EDS) mapping images of PdCo nanosheets demonstrated a uniform distribution of Pd and Co elements with a molar ratio of Pd/Co near 72:28 (Pd$_{72}$Co$_{28}$, Fig. 1f-h and Supplementary Fig. 2).

Electrocatalytic performances of Pd$_{72}$Co$_{28}$ nanosheets

The Pd$_{72}$Co$_{28}$ and Pd nanosheets were used as OER electrocatalysts in Li-O$_2$ batteries, respectively. Due to the larger specific surface area of Pd$_{72}$Co$_{28}$/C compared to Pd/C (Supplementary Fig. 3), more Li$_2$O$_2$ will deposit on the surface of Pd$_{72}$Co$_{28}$/C. Therefore, under full charge and discharge conditions, PdCo exhibited a discharge capacity of 7586 mAh/g$_{catalyst}$ (2.27 mAh/cm^2) at a current density of 0.1 A/g$_{catalyst}$
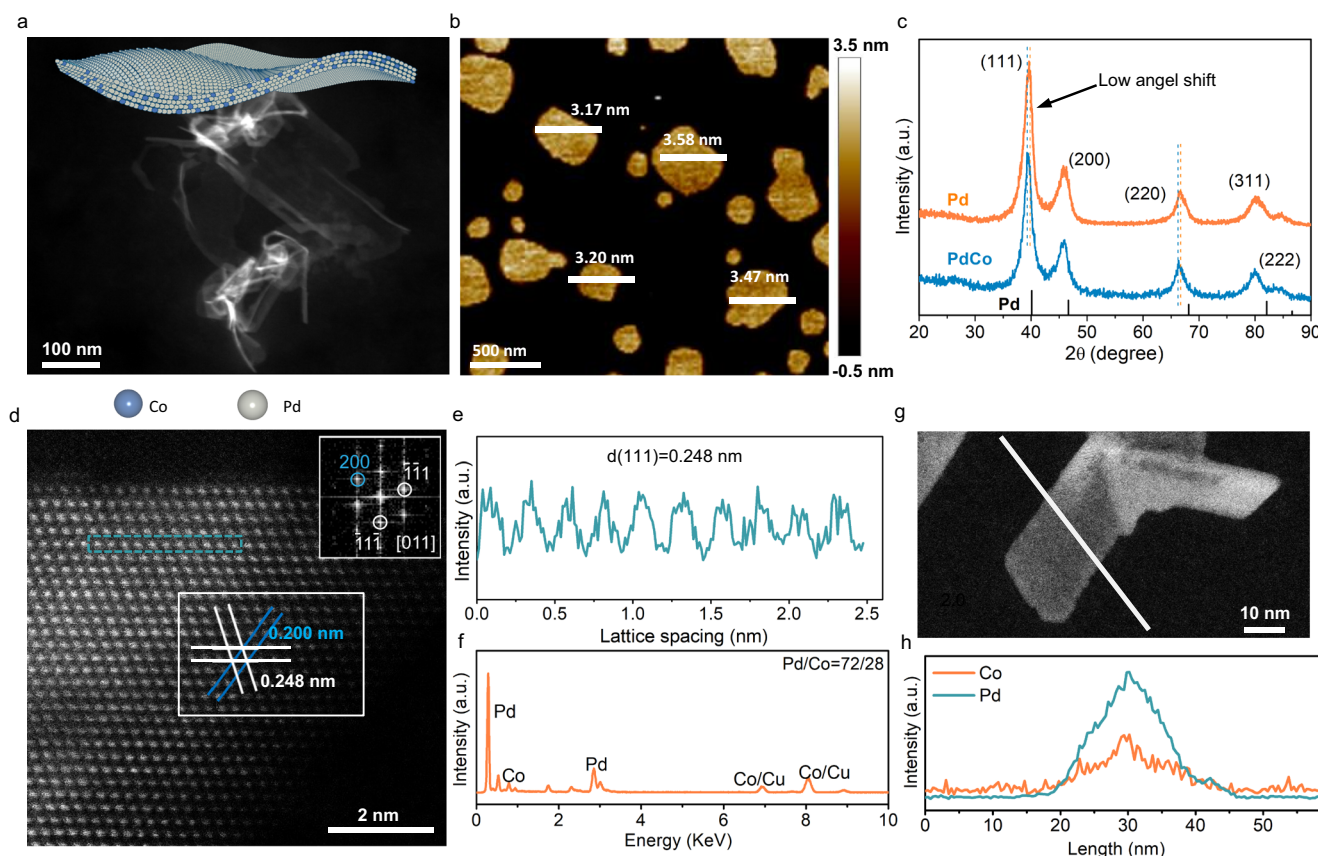

Fig. 1 | The characterization of PdCo nanosheets. a The HAADF-STEM images of PdCo nanosheets. **b** AFM images and a corresponding height of PdCo nanosheets. **c** XRD patterns of Pd and PdCo nanosheets. **d** Atomic-resolution HAADF-STEM image and FFT patterns of PdCo nanosheets. The inset is an FFT pattern of PdCo nanosheets from the white dash box. **e** Pixel intensity of PdCo from blue dash boxes in (**d**). **f** EDX spectra of PdCo nanosheets. **g, h** Linear elemental distribution of Pd and Co in PdCo nanosheets.
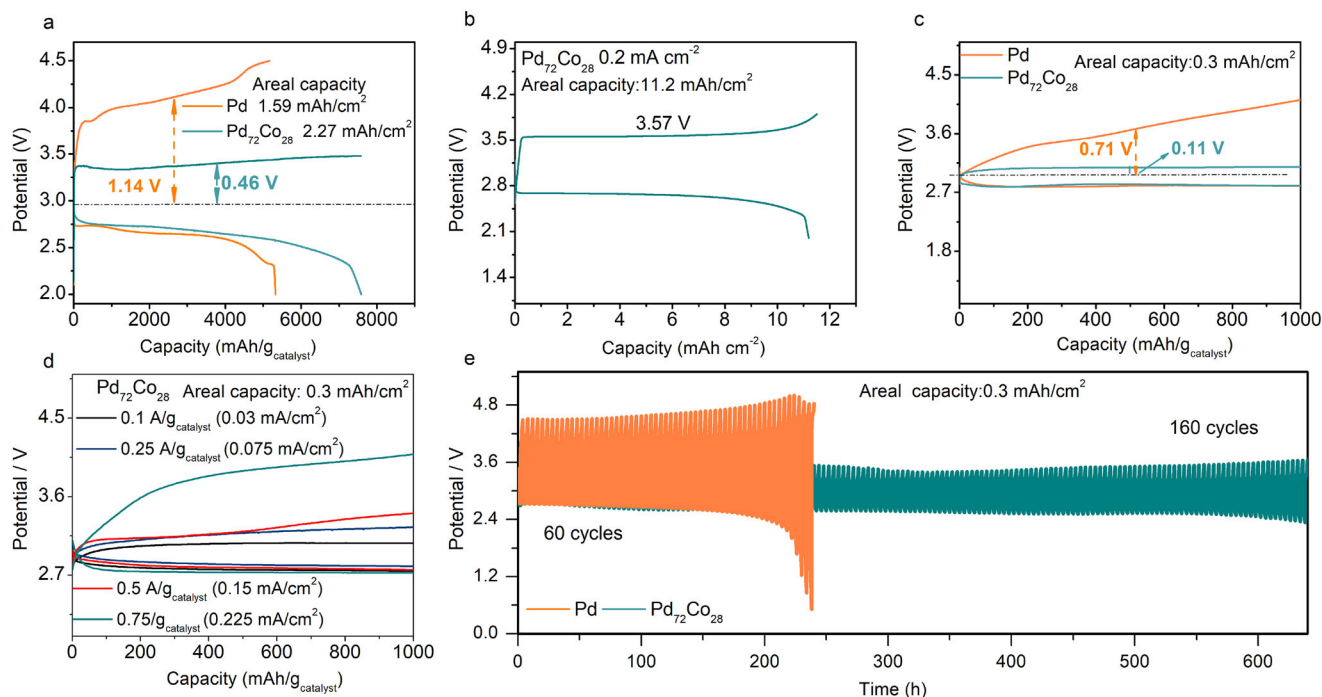
Fig. 2 | Performances of Pd and PdCo nanosheets. a The full discharge-charge profiles of Pd and $Pd_{72}Co_{28}$ nanosheets at a low loading mass (0.3 mg/cm²). **b** The full discharge-charge profiles of $Pd_{72}Co_{28}$ based at high loading mass (3 mg/cm²). **c** The charge-discharge curves of Pd and $Pd_{72}Co_{28}$ at a current density of 0.1 A/$g_{catalyst}$ (0.03 mA/cm²) with a limited capacity of 1000 mAh/$g_{catalyst}$ (0.3 mAh/ cm²). **d** Rate performance of $Pd_{72}Co_{28}$ nanosheets at a low loading mass of 0.3 mg/cm² and a low capacity of 0.3 mAh/cm². **e** Cycles performance of Pd and $Pd_{72}Co_{28}$ nanosheets with a limited capacity of 1000 mAh/$g_{catalyst}$ (0.3 mAh/cm²) at 0.5 A/$g_{catalyst}$ (0.15 mA/cm²).

(0.03 mA/cm²), surpassing that of the Pd (5325 mAh/$g_{catalyst}$ or 1.59 mAh/cm², Fig. 2a). It is noteworthy that as the charging voltage steadily increased to 4.5 V, the increased charging capacity was a result of electrolyte decomposition (Supplementary Figs. 4–6). Meanwhile, the $Pd_{72}Co_{28}$ electrocatalysts show a lower charge overpotentials of 0.46 V than that of Pd (1.14 V). When the loading mass of PdCo is increased to 3 mg/cm², the $Pd_{72}Co_{28}$ catalyst exhibits an areal capacity of 11.2 mAh/cm² (Fig. 2b), good rate performance (Supplementary Fig. 7), and an energy density of 1177 Wh/kg (including the mass of the catalysts, electrolytes, and Li_2O_2, as shown in Supplementary Table 1) according to the calculation method in the literature[38], far better than that of Li-ion batteries[39]. Meanwhile, the $Pd_{72}Co_{28}$ electrocatalyst can efficiently promote the decomposition of Li_2O_2 without any obvious parasitic products (Supplementary Figs. 8–12).

When the discharge capacity is restricted to 1000 mAh/$g_{catalyst}$ (0.3 mAh/cm²), $Pd_{72}Co_{28}$ demonstrated a remarkably low charge overpotential of 0.11 V with an energy conversion efficiency of 91% at a low loading mass (0.3 mg/cm²), outperforming Pd with an overpotential of 0.71 V (energy conversion efficiency: 76%, Fig. 2c). The cyclic voltammetry (CV) results demonstrated that the exchange current density of the $Pd_{72}Co_{28}$ surpassed that of pure Pd, confirming the good OER kinetics of $Pd_{72}Co_{28}$ (Supplementary Fig. 13). The rate performance further indicated that $Pd_{72}Co_{28}$ exhibited a low charge overpotential even at high current density of 0.75 A/$g_{catalyst}$ (0.225 mA/cm² in Fig. 2d), which was significantly advantageous compared to Pd (Supplementary Fig. 14). Such low charge overpotential of $Pd_{72}Co_{28}$ also demonstrated significant superiority over the reported OER electrocatalysts in $Li-O_2$ batteries (Supplementary Fig. 15 and Supplementary Table 2)[12,15,17,19,30,31,35,40–47]. Moreover, when the discharge capacity is limited to 1000 mAh/$g_{catalyst}$ (0.3 mAh/cm²), $Pd_{72}Co_{28}$ showed no noticeable degradation in the charge-discharge profiles after 160 cycles (640 h) at a current density is 0.5 A/$g_{catalyst}$ (0.15 mA/cm² in Fig. 2e). In contrast, Pd can only sustain cycling for 60 cycles

under the same conditions due to severe charge polarizations (Fig. 2e). It is worth noting that that although $Pd_{72}Co_{28}$ demonstrates low charge overpotential and good cycle stability at a low loading mass (0.3 mg cm⁻²) and a low depth of discharge (0.3 mAh cm⁻²), the performance of $Pd_{72}Co_{28}$ at high loading mass (3 mg cm⁻² or higher) and depths of discharge (11.2 mAh cm⁻² or higher) should be enhanced to meet the requirements of practical $Li-O_2$ batteries.

The reversibility analysis of $Pd_{72}Co_{28}$ nanosheet

To reveal the microstructure change of discharged $Pd_{72}Co_{28}$ nanosheets, the morphologies of $Pd_{72}Co_{28}$ and Pd were conducted by scanning electron microscopy (SEM). At a limited discharge capacity of 1000 mAh/$g_{catalyst}$ (0.3 mAh/cm²), the disk-shaped discharge products were observed on $Pd_{72}Co_{28}$ (Fig. 3a). These disk-shaped products (~0.7 μm) were identified as Li_2O_2 based on XRD patterns, Raman spectra, X-ray photoelectron spectroscopy (XPS) results, Fourier-transform infrared (FTIR) and nuclear magnetic resonance (NMR) spectra (Fig. 3b–d and Supplementary Figs. 16 and 17), which were different from the sphere-shape Li_2O_2 particles (~1.1 μm) with a slightly larger diameter on Pd (Fig. 3e and Supplementary Figs. 18–20). In comparison to Pd/C, the higher specific surface area of the $Pd_{72}Co_{28}$/C catalyst and the smaller size of the discharge products on the PdCo/C positive electrode facilitate good interface contact between Li_2O_2 and $Pd_{72}Co_{28}$/C according to the previous report[48–51], resulting in low charge transfer resistance (193 Ω in Supplementary Fig. 21 and Supplementary Table 3) and good OER kinetics for the $Pd_{72}Co_{28}$/C electrocatalyst.

The reversibility of $Pd_{72}Co_{28}$ and Pd catalysts in $Li-O_2$ batteries were analyzed through XRD patterns, Raman spectra, and XPS spectra under various discharge and charge cycling conditions. Throughout the 1st, 10th, 20th, 40th, and 100th cycles, the reversible formation and decomposition of Li_2O_2 are confirmed through XRD patterns and Raman spectra on $Pd_{72}Co_{28}$ (Fig. 3b, c). The good reversibility of
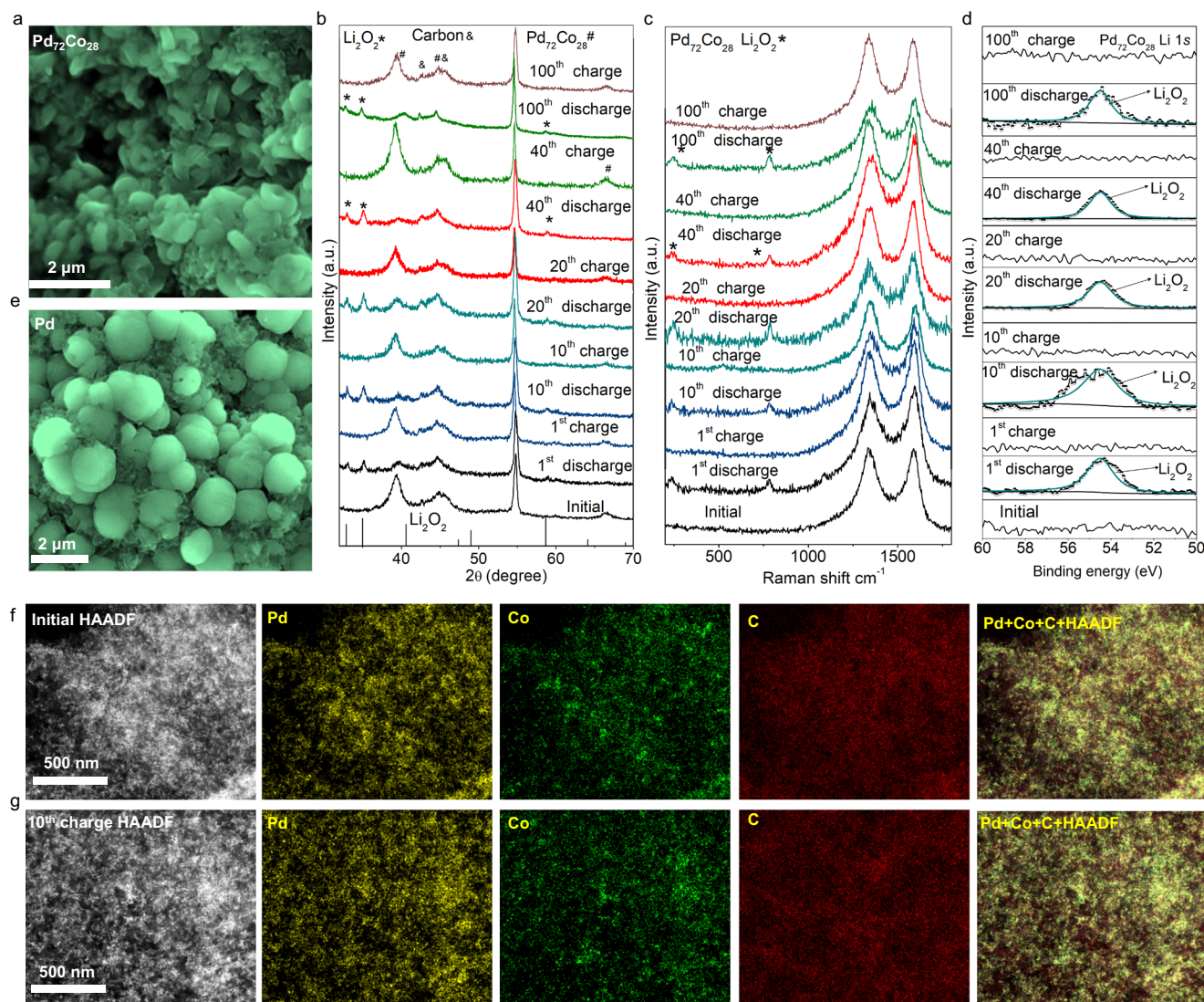
Fig. 3 | The reversibility analysis of PdCo nanosheets. a SEM images of 1st discharge $Pd_{72}Co_{28}$ nanosheets. **b–d** XRD patterns (**b**), Raman (**c**), and XPS (**d**) spectra of $Pd_{72}Co_{28}$ electrocatalysts at different cycles. **e** SEM images of 1st discharge Pd nanosheets. **f, g** Comparative TEM imaging and EDX elemental mapping in C, Pd, and Co distribution for $Pd_{72}Co_{28}$ electrocatalysts during the initial state (**f**) and the 10th cycle (**g**).

$Pd_{72}Co_{28}$ an also be confirmed by XPS results. Only Li 1s and C 1s spectra were utilized to identify the discharge products, considering the overlapping of O 1s signals from Li_2CO_3, Pd, and $Pd_{72}Co_{28}$ (Supplementary Figs. 22 and 23). Obviously, the reversible formation and decomposition of Li_2O_2 can be obtained on $Pd_{72}Co_{28}$ during 100 discharge-charge cycles (Fig. 3d and Supplementary Fig. 24). Moreover, no noticeable changes are observed in the oxidation states of Pd and Co in $Pd_{72}Co_{28}$ after 100th cycles, highlighting the good stability of the $Pd_{72}Co_{28}$ (Fig. 3f, g and Supplementary Figs. 25 and 26). In contrast, the high overpotential during the charging process of the Pd led to the formation of byproducts on Pd, including Li_2CO_3 and unreacted Li_2O_2, even in the 1st cycle (Supplementary Figs. 27 and 28).

The d-d orbital coupling between Pd and Co in $Pd_{72}Co_{28}$ nanosheets

Bader charge analysis was used to analyze the valence state changes of Pd in $Pd_{72}Co_{28}$ to elucidate the underlying mechanism for the outstanding OER catalytic activity of $Pd_{72}Co_{28}$ nanosheets. Due to the higher electron affinity of Pd than that of Co, electrons transferred from Co to Pd, resulting in a lower valence state of Pd in $Pd_{72}Co_{28}$

(Fig. 4a), which was in accordance with the XPS results (Supplementary Fig. 29). The charge transfer between Pd and Co was further confirmed by the analysis of differential charge density in two-dimension maps, revealing a higher electron density near pure Pd atoms than that of Pd atoms in $Pd_{72}Co_{28}$ nanosheets (Fig. 4b, c).

The electron transfer between Pd and Co ultimately resulted in a change of the density of state (DOS) for Pd in $Pd_{72}Co_{28}$ nanosheets compared to that of Pd nanosheets. For the pure Pd nanosheets in Fig. 4d, its Pd 4d-band was consisted of five distinct orbitals with varying energy levels, $4d_{z^2}$ (−1.79 eV), $4d_{x^2-y^2}$ (−1.87 eV), $4d_{xy}$ (−1.88 eV), $4d_{xz}$ (−1.90 eV) and $4d_{yz}$ (−1.90 eV). On the other hand, the Pd 4d-band in PdCo nanosheets exhibited increased electron localization, particularly noticeable in the $4d_{z^2}$ orbitals (Fig. 4e). Furthermore, the Pd $4d_{z^2}$ orbital in $Pd_{72}Co_{28}$ crossed the Fermi level, while the d_{xy}, d_{xz}, d_{yz}, d_{z^2}, and $d_{x^2-y^2}$ orbitals of both Pd and Co exhibited resonance within the energy ranges of approximately − 4 to − 2.7 eV, − 4 to − 2.4 eV, − 4 to −2.4 eV, − 4 to −1.8 eV, and − 4 to −1.6 eV, respectively, indicating a strong d-d orbital coupling between Pd and Co in $Pd_{72}Co_{28}$ (Fig. 4e). The d-d orbital interactions between Pd and Co ultimately led to orbital reconstruction and a decrease in the energy levels of Pd 4d-band in $Pd_{72}Co_{28}$. In comparison to the Pd 4d orbitals in pure Pd, the
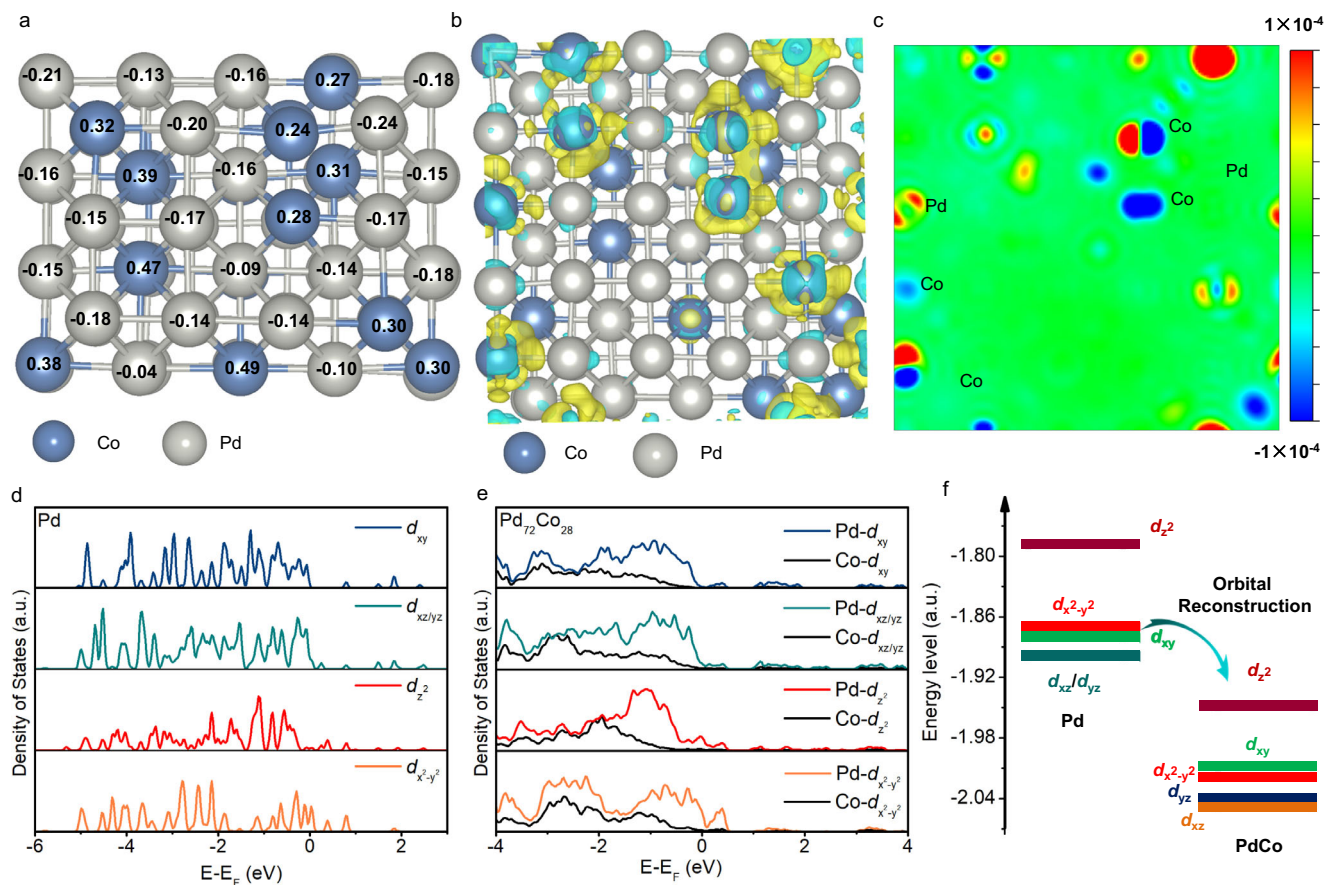
Fig. 4 | Electronic state analysis of Pd and Pd$_{72}$Co$_{28}$ nanosheets. a Bader charge results for Pd$_{72}$Co$_{28}$ nanosheets. **b** The differential charge density of Pd$_{72}$Co$_{28}$. The yellow and cyan areas indicate the gain and loss of electrons, respectively. **c** Two-dimensional charge density differences of Pd$_{72}$Co$_{28}$ nanosheets. The red and blue areas represent the gain and loss of electrons. **d** DOSs of Pd 4 d orbital for d_{xy}, $d_{yz/xz}$, d_{z^2}, and $d_{x^2-y^2}$ in Pd nanosheets. **e** DOSs of Pd and Co for d_{xy}, $d_{yz/xz}$, d_{z^2}, and $d_{x^2-y^2}$ in Pd$_{72}$Co$_{28}$ nanosheets. **f** Schematic diagram demonstrating the orbital reconstruction of Pd in Pd$_{72}$Co$_{28}$ compared to pure Pd nanosheets.

reconstructed Pd 4 d orbitals in Pd$_{72}$Co$_{28}$ underwent an energy splitting of d_{xz} and d_{yz}. Finally, the five independent Pd 4 d orbitals in PdCo were rearranged as d_{z^2} (−1.95 eV), d_{xy} (−2.01 eV), $d_{x^2-y^2}$ (−2.02 eV), d_{yz} (−2.04 eV), and d_{xz} (−2.05 eV) (Fig. 4f). Most interestingly, the top energy level of the reconstructed Pd 4 d_{z^2} in Pd$_{72}$Co$_{28}$ nanosheets was even lower the bottom energy level of Pd 4$d_{xz/yz}$ in Pd nanosheets. The decreased energy level Pd 4d in Pd$_{72}$Co$_{28}$ is also confirmed by the ultraviolet photoelectron spectroscopy (Supplementary Fig. 30), where Pd$_{72}$Co$_{28}$ exhibits a lower d-band center (−12.28 eV) than that of Pd (−11.84 eV).

The orbital interaction between adsorbed LiO$_2$ and Pd$_{72}$Co$_{28}$
Since the interaction between catalysts and intermediates is a key factor in determining OER catalytic performance, the orbital interactions between electrocatalysts (Pd$_{72}$Co$_{28}$ and Pd) and intermediates have been investigated. The DOSs of Pd d_{z^2} orbital and $d_{xz/yz}$ orbitals overlaps with the 5σ and 2π* orbitals of LiO$_2$, respectively (Fig. 5a, b), resulting in the formation of bonding orbitals (d_{z^2}-5σ and $d_{xz/yz}$-2π*) and antibonding orbitals ((d_{z^2}-5σ)* and ($d_{xz/yz}$-2π*)*). Considering the demonstrated orbital reconstruction and the energy level decrease, the antibonding orbitals exhibited a decrease in energy level when the 4 d_{xy}, 4d_{yz}, and 4d_{z^2} orbitals of Pd in Pd$_{72}$Co$_{28}$ interacted with the 2π* and 5σ orbitals of LiO$_2$, respectively (Fig. 5c, d). As a result, the electrons from Pd 4d orbitals intended to occupy the antibonding orbitals, leading to a weaker orbital interaction (−2.30 eV) between Pd$_{72}$Co$_{28}$ and LiO$_2$ compared to that of Pd (−2.67 eV). The weak adsorption interaction between Pd$_{72}$Co$_{28}$ and LiO$_2$ is further supported by ultraviolet-visible (UV-Vis) spectra (Supplementary Fig. 31), with

Pd$_{72}$Co$_{28}$ showing higher adsorption compared to Pd electrocatalysts. Additionally, the weak orbital interaction can also be confirmed through the analysis of the differential charge density and Bader charge results. The O atoms in LiO$_2$ connecting to Pd$_{72}$Co$_{28}$ exhibited higher oxidation states compared to Pd, indicating a less amount of electron transfer from Pd$_{72}$Co$_{28}$ to LiO$_2$ (0.11 e⁻ in Fig. 5e) relative to that of Pd (1.02 e⁻ in Fig. 5f).

The weak orbital interaction between Pd$_{72}$Co$_{28}$ and LiO$_2$ enhanced the OER electrocatalytic activity, as confirmed by the Gibbs free energy results. The OER overpotential is defined as $\eta_{OER} = U_c − U_{eq}$. Here, U_{eq} represents the equilibrium potential of the overall reaction, while U_c indicates the minimum potential at which the Gibbs free energy gradually increases during the charge process. Furthermore, U_0 represents the Gibbs free energy of the relevant species when the potential is 0. During the charging process, superoxide species are identified as intermediates for Pd and Pd$_{72}$Co$_{28}$ electrocatalysts based on UV-Vis results, confirming that the decomposition of Li$_2$O$_2$ proceeds in two steps (Supplementary Figs. 32 and 33). For both Pd and Pd$_{72}$Co$_{28}$, the rate-determining steps of the OER process involve the oxidation of LiO$_2$ to O$_2$ and Li⁺. Therefore, the weak orbital interaction between Pd$_{72}$Co$_{28}$ and LiO$_2$ led to lower activation energy (0.5 eV in Fig. 5h) than that of Pd nanosheets (0.8 eV in Fig. 5g), which is consistent with the electrochemical impedance spectra (EIS) (Supplementary Fig. 34). The lower activation energy of Pd$_{72}$Co$_{28}$ indicates a low charge overpotentials of Pd$_{72}$Co$_{28}$ (0.5 V) relative to that of Pd nanosheets (0.8 V). This result was also apparent in the phase diagram, where the intersection of LiO$_2$ and O$_2$ occurred at 3.47 V for Pd$_{72}$Co$_{28}$ and 4.00 V for Pd, respectively (Fig. 5i).
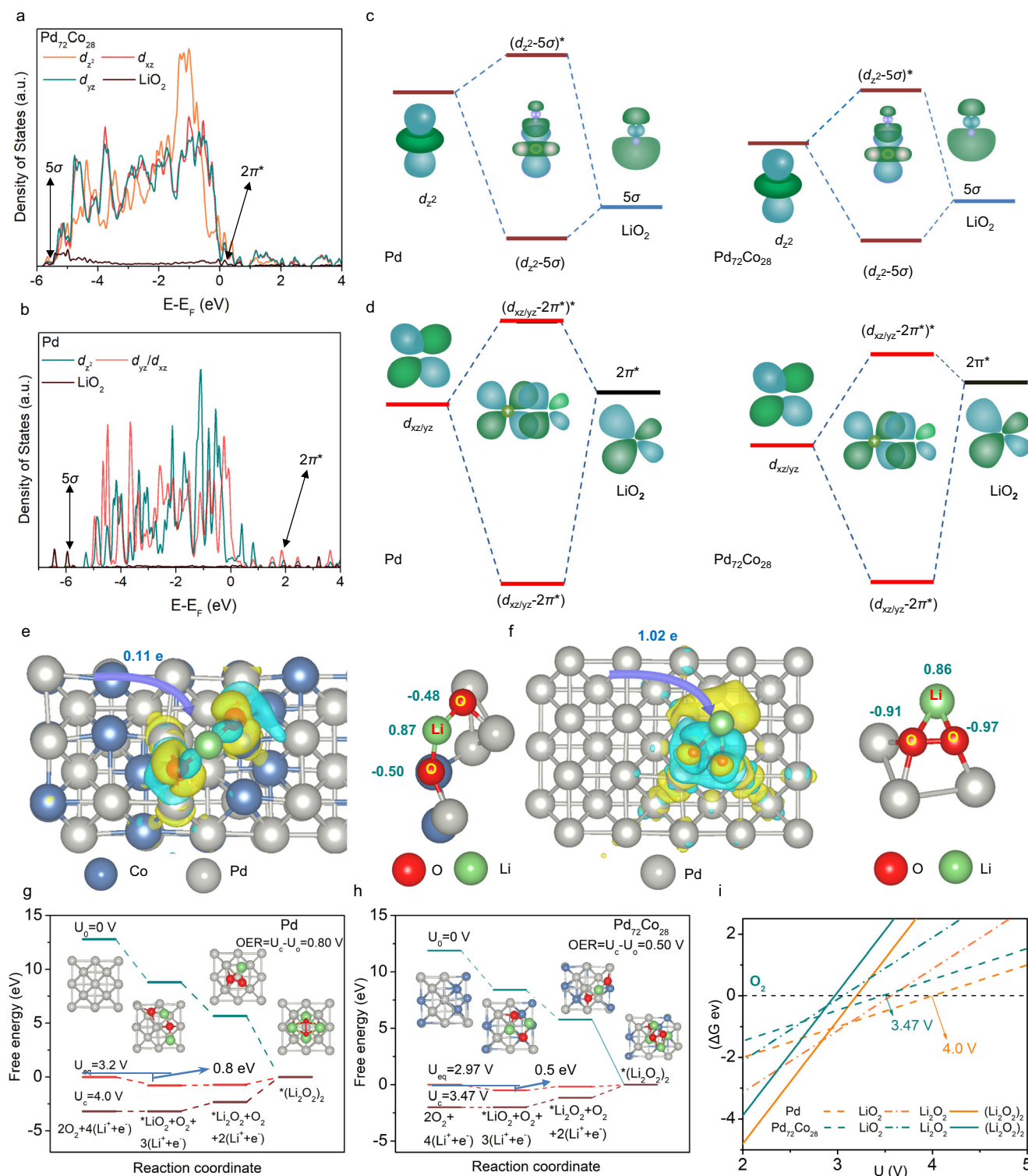
Fig. 5 | The orbital interaction between adsorbed LiO$_2$ and catalyst (Pd and Pd$_{72}$Co$_{28}$), and Gibbs free energy profiles. a, b The DOSs for the orbital hybridization between Pd 4d orbitals and adsorbed LiO$_2$ for Pd (**a**) and Pd$_{72}$Co$_{28}$ (**b**). **c, d** A schematic representation of the hybridization between LiO$_2$ and Pd (or Pd$_{72}$Co$_{28}$) 4d orbitals. **e, f** The difference charge density of LiO$_2$ adsorption on Pd$_{72}$Co$_{28}$ (**e**) and Pd (**f**), visualized using an isosurface of 0.005 e/Bohr^3. The yellow and cyan isosurfaces indicate the gain and loss of electrons, respectively. **g, h** The Gibbs free energy profiles of Pd$_{72}$Co$_{28}$ and Pd at various potentials. **i** Phase diagram of the positive electrode reaction on the Pd and Pd$_{72}$Co$_{28}$.

Three different contents of Co in PdCo catalysts (Pd$_{81}$Co$_{19}$, Pd$_{72}$Co$_{28}$, and Pd$_{56}$Co$_{44}$) are prepared to further investigate the effect of Co content on the charge overpotential in Li-O$_2$ batteries (Supplementary Figs. 35 and 36). The charge overpotential of the PdCo catalyst is mainly determined by two factors: the OER activity

of the Pd atom and the number of Pd sites. With a slight increase in the Co content from Pd$_{81}$Co$_{19}$ to Pd$_{72}$Co$_{28}$, the d-band center of Pd in Pd$_{72}$Co$_{28}$ (−12.28 eV) shifts downward compared to Pd$_{81}$Co$_{19}$ (−11.92 eV, Supplementary Fig. 37), suggesting weaker adsorption towards LiO$_2$ and enhanced OER catalytic activities of Pd in Pd$_{72}$Co$_{28}$.

Hence, despite a slight reduction in the number of active Pd sites, the moderate increase of Co content results in a lower overpotential for $Pd_{72}Co_{28}$ (0.11 V) compared to $Pd_{81}Co_{19}$ (0.53 V, Supplementary Fig. 38) at a low loading mass (0.3 mg/cm²) with a low capacity (0.3 mAh/cm²). With a further increase in the Co content from $Pd_{72}Co_{28}$ to $Pd_{56}Co_{44}$, although the decreased d-band center of $Pd_{56}Co_{44}$ (− 13.12 eV, Supplementary Fig. 37) enhances the OER activity of Pd, the significant decrease in the number of Pd sites results in a higher charge overpotential for $Pd_{56}Co_{44}$ (0.38 V, Supplementary Figs. 38) compared to $Pd_{72}Co_{28}$ (0.11 V) at a low loading mass (0.3 mg/cm²) with a low capacity (0.3 mAh/cm²). Therefore, the $Pd_{72}Co_{28}$ catalyst with a moderate Co content can guarantee relatively high OER catalytic activity and a significant number of Pd sites, resulting in low charge overpotential.

Discussion

In summary, an orbital reconstruction strategy has been reported in $Pd_{72}Co_{28}$ nanosheets as a highly efficient electrocatalyst in Li-O_2 batteries with a low charge overpotential of 0.11 V at a low loading mass (0.3 mg/cm²) and a low capacity (0.3 mAh/cm²). Experimental results and theoretical calculations revealed that the d-d orbital coupling between Pd and Co in $Pd_{72}Co_{28}$ nanosheets leads to Pd $4d$ orbital reconstruction and significantly reduced the energy levels of the electrochemical active $4d_{xy}$, $4d_{yz}$, and $4d_{z^2}$ orbitals of Pd rather than the only band center shift in the conventional approaches. As a result, the interactions between the energetically lowered $4d_{xy}/4d_{yz}/4d_{z^2}$ orbitals of Pd in $Pd_{72}Co_{28}$ and $2\pi^*/5\sigma$ orbitals of LiO_2 optimized the activation energy of the rate-determining step and enhanced the OER kinetics. This study developed a highly efficient Li-O_2 batteries with a reported highest energy conversion efficiency of 91%, and offered a guideline for the precise manipulation of d orbitals in designing efficient noble metal-based electrocatalysts.

Methods

Chemicals and materials

Palladium(II) acetylacetonate (Pd(acac)$_2$, ≥ 99.95%), cobalt(II) acetylacetonate (Co(acac)$_2$, ≥ 97%), molybdenum carbony (Mo(CO)$_6$, ≥ 98%), oleylamine (C$_{18}$H$_{37}$N, 80–90%), cyclohexane (C$_6$H$_{12}$, ≥ 99.9%), ethanol (C$_2$H$_5$OH, ≥ 99.7%), acetic acid (CH$_3$COOH, ≥ 99.5%), dimethyl sulfoxide (C$_2$H$_6$SO, ≥ 99.9%), 1-methyl-2-pyrrolidone (NMP, C$_6$H$_{13}$NO, ≥ 99.5%), tetraethylene glycol dimethyl ether (C$_{10}$H$_{22}$O$_5$, 99%) were purchased from Macklin. Poly(vinylidene fluoride) (PVDF, average molecular weight -275000), lithium trifluoromethanesulfonate (LiCF$_3$SO$_3$, ≥ 99.5%), and lithium foil (thickness of 0.4 mm, diameter of 16 mm, ≥ 99.9%) were obtained from Aladdin. Carbon paper (thickness of 0.21 mm, resistivity of 8 mΩ cm²) was purchased from Shanghai Hesen. A separator (thickness of 0.26 mm, diameter of 18 mm) was purchased from Whatman. The pure O$_2$ (99.5%) was obtained from Linde HKO Ltd. XC72R carbon(≥ 98%) was purchased from Energy. Parafilm (thickness of 127 μm) was purchased from Bemis. To ensure the reliability and reproducibility of the experimental results, all experiments were independently repeated at least three times.

Synthesis of Pd and PdCo ($Pd_{81}Co_{19}$, $Pd_{72}Co_{28}$, and $Pd_{56}Co_{44}$) nanosheets

10 mg of Pd(acac)$_2$, 10 mg of Co(acac)$_2$, and 30 mg of Mo(CO)$_6$ were dissolved in 5 mL of oleylamine, followed by sonicating for 2 h to ensure uniform dispersion. Next, the solution underwent a 5 h reaction in a 180 °C oil bath. After the completion of the reaction and cooling to room temperature, the product was collected by centrifugation. Subsequently, the product underwent three rounds of centrifugal washing using a mixture of cyclohexane and ethanol (in a 9:1 volume ratio) to obtain the $Pd_{72}Co_{28}$. The synthesis of $Pd_{81}Co_{19}$ and $Pd_{56}Co_{44}$ is similar to that of $Pd_{72}Co_{28}$, differing only in the amount of metal salts added.

To synthesize $Pd_{81}Co_{19}$, 10 mg of Pd(acac)$_2$ and 5 mg of Co(acac)$_2$ are needed, whereas for $Pd_{56}Co_{44}$, 8 mg of Pd(acac)$_2$ and 12 mg of Co(acac)$_2$ are required. In addition, the synthesis process for Pd nanosheets closely resembles that of $Pd_{72}Co_{28}$, with the only difference being the exclusion of Co(acac)$_2$ as a required component.

Preparation of Pd/C and PdCo/C ($Pd_{81}Co_{19}$/C, $Pd_{72}Co_{28}$/C, and $Pd_{56}Co_{44}$/C)

The synthesized PdCo nanosheets (80 mg) was dispersed in cyclohexane (60 mL), followed by homogeneous mixing with XC72R carbon (20 mg), and subjected to continuous sonication for 60 min. The products were obtained by centrifugation and subsequent washing with a mixed solvent of cyclohexane/ethanol (9/1, v/v). Subsequently, the products was continuously stirred overnight with the addition of acetic acid to remove any residual surfactants. Finally, the resulting product PdCo/C was obtained through centrifugation. The loading mass of PdCo in PdCo/C was 80.0 wt%. The synthesis process for Pd/C was the same as that for PdCo/C.

Characterizations

The crystal structures of both Pd and PdCo were investigated using a powder X-ray diffraction (XRD, a Bruker D2 Phaser XE-T X-ray diffractometer) utilizing Cu Kα radiation (λ = 1.5406 Å). The microstructural features of Pd and PdCo were examined through high-resolution transmission electron microscopy (HR-TEM) using the Tecani-G2 T20 instrument and field-emission scanning electron microscopy (SEM) employing the Thermo Fisher Quattro S system. The discharge products of Pd and PdCo were identified by FT-IR using a PerkinElmer Spectrum Two Spectrometer with the wavenumber range of 400–4000 cm^{-1} and NMR (Bruker). The valence bands of Pd and PdCo were analyzed by ultraviolet photoelectron spectroscopy (UPS, Thermo escalab 250Xi). Raman spectroscopy was employed to analyze the discharge products of Pd and PdCo, which was conducted using a WITec alpha 300 Raman System equipped with a 532 nm wavelength laser. X-ray photoelectron spectroscopy (XPS) measurements were performed using a Thermo Fisher ESCALAB XI + instrument to investigate the valence states of Pd in Pd and PdCo, and discharge products during the cycling process. Prior to ex situ measurements, the discharged or charged PdCo or Pd positive electrodes were transferred to an Ar-filled glovebox and disassembled at a temperature of 20 °C, with both O$_2$ and H$_2$O concentrations in the glovebox maintained below 0.1 ppm. The PdCo (or Pd) positive electrodes were washed by dimethyl sulfoxide to remove residual electrolytes and salts. Subsequently, the PdCo or Pd positive electrode was tightly wrapped with Parafilm to prevent contamination. To ensure the accuracy of the characterization results, the positive electrode sample was taken out of the glovebox 5 min before performing ex situ characterizations.

Battery assembly and performances

In order to fabricate the positive electrode (PdCo/C) for Li-O_2 batteries, the 10 wt% poly(vinylidene fluoride) binder was dispersed in NMP under continuous magnetic stirring. Subsequently, the PdCo/C (90 wt%) was transferred into the PVDF solution and further stirred for 8 h. Then, the obtained slurry was drop-casted onto a carbon paper current collector (thickness of 0.21 mm, a diameter of 10 mm) using a pipette, followed by vacuum drying at 60 °C for 24 h to obtain the PdCo/C electrode. The carbon paper current collector discs were obtained by cutting the carbon paper using a slicing machine (Shenzhen Kejing, Model: MSK-T10). In addition, Pd/C electrocatalysts were utilized as a positive electrode for comparative analysis. The loading mass for both PdCo/C and Pd/C ranges from 0.3 to 3 mg/cm². A 2032 coin cell with 13 holes was assembled in a glove box under an Ar atmosphere, where the content of both H$_2$O and O$_2$ were below 0.1 ppm. The cell configuration included a positive electrode, a

lithium foil (Aladdin, thickness of 0.4 mm, a diameter of 16 mm), a separator (Whatman, thickness of 0.26 mm, dimension of 18 mm), and solvent (10 μL, 1 M lithium trifluoromethanesulfonate in tetra-ethylene glycol dimethyl ether). The cell assembly was conducted using a hydraulic crimping machine (Shenzhen kejing, Model: MSK-110). The lithium foil was prepared prior to cell assembly. Prior to battery measurements, the assembled Li-O$_2$ batteries were placed into a container filled with ultra-pure dry O$_2$ (99.99%, 1.0 atm.) and left to stand in a constant-temperature chamber with convection heating (25 °C, Neware, Model: MIHW-200-160CH) for 24 h. Following that, galvanostatic experiments were conducted on the battery using a LAND cell system. The cyclic voltammogram was carried out using an electrochemical workstation (CHI760e) from 2.0 to 4.5 V at 0.3 mV/s. EIS was analyzed by a CHI760E workstation, with an amplitude voltage of 10 mV and a frequency range from 10^5 Hz to 0.1 Hz (number of data points: 31). The system was held at open-circuit voltage for 10 min prior to electrochemical impedance spectroscopy (EIS) measurements. Each electrochemical data was analyzed based on the measurements of three cell samples.

DFT calculations

The DFT calculations were performed using the Vienna Ab initio simulation package (VASP). We adopted the generalized gradient approximation of Perdew-Burke-Ernzerhof (GGA-PBE) to characterize the exchange-correlation potential in our calculations. To account for the interactions between ion cores and valence electrons, the projector augmented-wave (PAW) method was utilized. A fixed plane-wave cutoff energy of 450 eV was applied in the calculations. The structural models were relaxed until achieving Hellmann-Feynman forces below − 0.02 eV/Å and an energy change below 10^{-5} eV. To account for dispersion interactions between all atoms in the adsorption models, Grimme's DFT-D3 methodology was employed. The optimized configuration of Pd and Pd$_{72}$Co$_{28}$ are shown in Supplementary Data 1, 2.

Data availability

The data that support the conclusions of this study are available within the paper and Supplementary information. The DOI for the dataset on Figshare is https://doi.org/10.6084/m9.figshare.27683289. Source data are provided in this paper.

References
1. Ye, H. & Li, Y. A perspective on sulfur-equivalent cathode materials for lithium-sulfur batteries. *Energy Lab* **1**, 220003-220001–220003-220009 (2023).
2. Peng, J., Yi, X., Fan, L., Zhou, J. & Lu, B. Molecular extension engineering constructing long-chain organic elastomeric interphase towards stable potassium storage. *Energy Lab* **1**, 220014-220011–220014-220017 (2023).
3. Zaidi, S. S. H. & Li, X. Li–O$_2$/air batteries using ionic liquids–a comprehensive review. *Adv. Energy Mater.* **13**, 2300985 (2023).
4. Askins, E. J. et al. Triarylmethyl cation redox mediators enhance Li–O$_2$ battery discharge capacities. *Nat. Chem.* **15**, 1247–1254 (2023).
5. Tian, J. et al. Sabatier relations in electrocatalysts based on high-entropy alloys with wide-distributed d-band centers for Li-O$_2$ batteries. *Angew. Chem. Int. Ed.* **62**, e202310894 (2023).
6. Han, X., Zhao, L., Wang, J., Liang, Y. & Zhang, J. Delocalized electronic engineering of Ni$_5$P$_4$ nanoroses for durable Li–O$_2$ batteries. *Adv. Mater.* **35**, 2301897 (2023).
7. Bai, T. et al. Atomic Ni-catalyzed cathode and stabilized Li metal anode for high-performance Li–O$_2$ batteries. *eScience* **5**, 100310 (2025).
8. Jia, C. et al. Bifunctional photoassisted Li–O$_2$ battery with ultrahigh rate-cycling performance based on siloxene size regulation. *ACS Nano* **17**, 1713–1722 (2023).
9. He, Y. et al. A "Trinity" design of Li-O$_2$ battery engaging the slow-release capsule of redox mediators. *Adv. Mater.* **35**, 2308134 (2023).
10. Liu, Y. et al. Tailoring the adsorption behavior of superoxide intermediates on nickel carbide enables high-rate Li–O$_2$ batteries. *eScience* **2**, 389–398 (2022).
11. Cai, Y. et al. Ionic liquid electrolyte with weak solvating molecule regulation for stable Li deposition in high-performance Li–O$_2$ batteries. *Angew. Chem. Int. Ed.* **135**, e202218014 (2023).
12. Zhou, Y. et al. Cascaded orbital–oriented hybridization of intermetallic Pd$_3$Pb boosts electrocatalysis of Li–O$_2$ battery. *Proc. Natl. Acad. Sci. USA* **120**, e2301439120 (2023).
13. Liang, Y. L. et al. A rotating cathode with periodical changes in electrolyte layer thickness for high-rate Li–O$_2$ batteries. *Adv. Mater.* **36**, 2403230 (2024).
14. Xiao, F. et al. D-band center regulation for durable catalysts and constructing a robust hybrid layer on Li anode enable long-life Li-O$_2$ batteries. *Adv. Energy Mater.* **14**, 2303766 (2024).
15. Zhou, Y. et al. Engineering e$_g$ orbital occupancy of Pt with Au alloying enables reversible Li–O$_2$ batteries. *Angew. Chem. Int. Ed.* **61**, e202201416 (2022).
16. Hong, J., Hyun, S., Tsipoaka, M., Samdani, J. S. & Shanmugam, S. RuFe alloy nanoparticle-supported mesoporous carbon: efficient bifunctional catalyst for Li–O$_2$ and Zn–air batteries. *ACS Catal.* **12**, 1718–1731 (2022).
17. Zhang, E. et al. Electron localization in rationally designed Pt$_1$Pd single-atom alloy catalyst enables high-performance Li–O$_2$ batteries. *J. Am. Chem. Soc.* **146**, 2339–2344 (2024).
18. Zheng, L.-J. et al. Regulating electrochemistry kinetics and discharge product selectivity with near-free cobalt single-atom catalyst in Li–O$_2$ batteries. *Energy Storage Mater.* **56**, 331–341 (2023).
19. Hu, X. et al. Ru single atoms on N-doped carbon by spatial confinement and ionic substitution strategies for high-performance Li–O$_2$ batteries. *J. Am. Chem. Soc.* **142**, 16776–16786 (2020).
20. Zhang, Y. et al. Single-atom-mediated spinel octahedral structures for elevated performances of Li-oxygen batteries. *Angew. Chem. Int. Ed.* **135**, e202218926 (2023).
21. Bai, T. et al. Recent progress on single-atom catalysts for lithium–air battery applications. *Energy Environ. Sci.* **16**, 1431–1465 (2023).
22. Li, D. et al. Activating MoS$_2$ nanoflakes via sulfur defect engineering wrapped on CNTs for stable and efficient Li-O$_2$ batteries. *Adv. Funct. Mater.* **32**, 2108153 (2022).
23. He, B. et al. MoSe$_2$@CNT core-shell nanostructures as grain promoters featuring a direct Li$_2$O$_2$ formation/decomposition catalytic capability in lithium-oxygen batteries. *Adv. Energy Mater.* **11**, 2003263 (2021).
24. Lin, X. et al. An open-structured matrix as oxygen cathode with high catalytic activity and large Li$_2$O$_2$ accommodations for lithium-oxygen batteries. *Adv. Energy Mater.* **8**, 1800089 (2018).
25. Cao, D. et al. Crystal phase-controlled modulation of binary transition metal oxides for highly reversible Li–O$_2$ batteries. *Nano Lett.* **21**, 5225–5232 (2021).
26. Agyeman, D. A. et al. Synergistic catalysis of the lattice oxygen and transition metal facilitating ORR and OER in perovskite catalysts for Li–O$_2$ batteries. *ACS Catal.* **11**, 424–434 (2020).
27. Sun, Z. et al. Synergized multimetal oxides with amorphous/crystalline heterostructure as efficient electrocatalysts for lithium–oxygen batteries. *Adv. Energy Mater.* **11**, 2100110 (2021).
28. Yuan, M. et al. Ultrathin two-dimensional metal–organic framework nanosheets with the inherent open active sites as electrocatalysts in aprotic Li–O$_2$ batteries. *ACS Appl. Mater. Interfaces* **11**, 11403–11413 (2019).
29. Zhou, Y. et al. Orbital coupling of PbO$_7$ node in single-crystal metal–organic framework enhances Li-O$_2$ battery electrocatalysis. *Nano Lett.* **23**, 10600–10607 (2023).

30. Lv, Q. et al. Atomic ruthenium-riveted metal–organic framework with tunable d-band modulates oxygen redox for Lithium–oxygen batteries. *J. Am. Chem. Soc.* **144**, 23239–23246 (2022).

31. Lv, Q., Zhu, Z., Ni, Y., Geng, J. & Li, F. Spin-state manipulation of two dimensional metal-organic framework with enhanced metal-oxygen covalency for lithium-oxygen batteries. *Angew. Chem. Int. Ed.* **61**, e202114293 (2022).

32. Tian, S. L. et al. A force-assisted Li–O$_2$ battery based on piezo-electric catalysis and band bending of MoS$_2$/Pd cathode. *Adv. Energy Mater.* **14**, 2303215 (2024).

33. Zheng, J. et al. Single-atom Pd-N$_4$ catalysis for stable low-overpotential lithium-oxygen battery. *Small* **19**, 2204559 (2023).

34. Guo, L. et al. Pd cluster decorated free standing flexible cathode for high performance Li-oxygen batteries. *Nano Res.* **17**, 2678–2686 (2024).

35. Zhou, Y. et al. Lewis-acidic PtIr multipods enable high-performance Li–O$_2$ batteries. *Angew. Chem. Int. Ed.* **60**, 26592–26598 (2021).

36. Cao, C. et al. Mechanistic insight into the synergetic catalytic effect of Pd and MnO$_2$ for high-performance Li–O$_2$ cells. *Energy Storage Mater.* **12**, 8–16 (2018).

37. Li, K., Dong, H., Wang, Y., Yin, Y. & Yang, S. Preparation of low-load Au-Pd alloy decorated carbon fibers binder-free cathode for Li-O$_2$ battery. *J. Colloid Interface Sci.* **579**, 448–454 (2020).

38. Liang, Z., Wang, W. & Lu, Y.-C. The path toward practical Li-air batteries. *Joule* **6**, 2458–2473 (2022).

39. Jenkins, M. et al. A high capacity gas diffusion electrode for Li–O$_2$ batteries. *Adv. Mater.* **36**, 2405715 (2024).

40. Wang, P. et al. Atomically dispersed cobalt catalyst anchored on nitrogen-doped carbon nanosheets for lithium-oxygen batteries. *Nat. Commun.* **11**, 1576 (2020).

41. Lu, J. et al. A lithium–oxygen battery based on lithium superoxide. *Nature* **529**, 377–382 (2016).

42. Song, L.-N. et al. Tuning lithium-peroxide formation and decomposition routes with single-atom catalysts for lithium–oxygen batteries. *Nat. Commun.* **11**, 2191 (2020).

43. Ke, S.-W. et al. Covalent organic frameworks with Ni-Bis (dithiolene) and Co-porphyrin units as bifunctional catalysts for Li-O$_2$ batteries. *Sci. Adv.* **9**, eadf2398 (2023).

44. Zhang, J. et al. A long-life lithium-oxygen battery via a molecular quenching/mediating mechanism. *Sci. Adv.* **8**, eabm1899 (2022).

45. Zhang, L. et al. Metal telluride nanosheets by scalable solid lithiation and exfoliation. *Nature* **628**, 313–319 (2024).

46. Asadi, M. et al. A lithium–oxygen battery with a long cycle life in an air-like atmosphere. *Nature* **555**, 502–506 (2018).

47. Xiong, Q. et al. Hydrogen-bond-assisted solution discharge in aprotic Li–O$_2$ batteries. *Adv. Mater.* **34**, 2110416 (2022).

48. Chen, Y. et al. Metal-air batteries: progress and perspective. *Sci. Bull.* **67**, 2449–2486 (2022).

49. Shi, W. et al. High-entropy alloy stabilized and activated Pt clusters for highly efficient electrocatalysis. *SusMat* **2**, 186–196 (2022).

50. Liu, L., Zhou, C., Fang, W., Hou, Y. & Wu, Y. Rational design of Ru/TiO$_2$/CNTs as cathode: promotion of cycling performance for aprotic lithium-oxygen battery. *Energy Mater.* **3**, 300011 (2023).

51. Zhou, Y. & Guo, S. Recent advances in cathode catalyst architecture for lithium–oxygen batteries. *eScience* **3**, 100123 (2023).

Acknowledgements

Author contributions

Y.Z. and K.Y. contributed equally to this work. S.G., and G.H. conceived the project. G.H. and W.Z. secured funding and supervised the project. Y.Z., K.Y., Y.H., J.L., A.Z., D.L., and G.G. finished the catalysts preparation, characterizations, performance testing, and DFT calculations. J.Z., Kai L., T.Z., Kunlun L., C.L., H.Y., and H.C. contributed to the analysis of the experimental data and participated in the result discussion. Y.Z. wrote the manuscript. G.H., S.G., and W.Z. revised the manuscript. All the authors commented on the final manuscript.

Competing interests

The authors declare no competing interests.

Additional information